

Radioastrometry at different frequencies

LEONID PETROV¹

¹*NASA Goddard Space Flight Center
Code 61A1, 8800 Greenbelt Rd, Greenbelt, 20771 MD, USA*

(Received April 12, 2024; Revised; Accepted)

Submitted to AJ

ABSTRACT

Very long baseline interferometry (VLBI) technique allows us to determine positions of thousands of radio sources using the absolute astrometry approach. I have investigated the impact of a selection of observing frequencies in a range from 2 to 43 GHz in single-band, dual-band, and quad-band observing modes on astrometric results. I processed seven datasets in a range of 72 thousands to 6.9 million observations, estimated source positions, and compared them. I found that source positions derived from dual-band, quad-band, and 23.6 GHz single-band data agree at a level below 0.2 mas. Comparison of independent datasets allowed me to assess the error level of individual catalogues: 0.05–0.07 mas per position component. Further comparison showed that individual catalogues have systematic errors at the same level. Positions from 23.6 GHz single-band data show systematic errors related to the residual ionosphere contribution. Analysis of source positions differences revealed systematic errors along jet directions at a level of 0.09 mas. Network related systematic errors affect all the data regardless of frequency. Comparison of position estimates allowed me to derive the stochastic error model that closes the error budget. Based on collected evidence, I made a conclusion that a development of frequency-dependent reference frames of the entire sky is not warranted. In most cases dual-band, quad-band, and single-band data at frequency 22 GHz and higher can be used interchangeably, which allows us to exploit the strength of a specific frequency setup for given objects. Mixing observations at different frequencies causes errors not exceeding 0.07 mas.

Keywords: astrometry — catalogues — surveys

1. INTRODUCTION

The method of very long baseline interferometry (VLBI) first proposed by Matveenko et al. (1965) turned out a powerful tool for geodesy and astronomy. Analysis of VLBI regular campaigns that run since 1980s allowed us to determine positions and velocities of observing stations, time series of the Earth orientation parameters, and coordinates of observed sources, including artificial satellites. VLBI

hardware allows us to operate at frequencies from 20 MHz to 230 GHz, and most of the stations have the capability to tune observing frequencies or observe several frequencies simultaneously within a certain range. Therefore, we have a freedom to select a frequency range when plan observations. A question emerges: which frequency range should we select? I will limit further discussion to a case of absolute astrometry based on processing total group delays. Since path delay is proportional to the dot product of the baseline vector and the unit source vector, source position accuracy does

not depend on frequency directly. In the absence of systematic errors, it is proportional to the precision of derived group delays and reciprocal to the baseline length. In that ideal case if one wants to reach the highest positional accuracy, observations need to be done at a network with longest baselines, at frequencies where a given source has the strongest flux density, and using such a setup that provides the widest spanned bandwidth.

However, systematic errors often dominate the error budget. The most relevant systematic errors are those that are caused by mismodeling path delay in the neutral atmosphere, mismodeling the ionospheric contribution, errors caused by source structure, and a core shift.

Path delay in the neutral atmosphere virtually does not depend on frequency in a range of 1 to 1000 GHz. But even if path delay itself does not depend on frequency, our ability to estimate residual path delay with respect to the a priori does depend. A robust estimation of the atmospheric path delay in zenith direction requires observing sources at both high and low elevations. MacMillan & Ma (1994) found that the systematic errors reach the minimum when observations at elevation angles 7° are included. At frequencies above 15 GHz atmospheric opacity becomes noticeable. If the atmospheric opacity is 0.5 in the zenith direction, it can reach 2.5–3.0 at 10° elevation. That means flux density in the zenith direction is attenuated by a factor of 1.4, while at 10° elevation it is attenuated by a factor of 15–20. We may not be able to detect a source because of such a strong attenuation.

The impact of the ionosphere is reciprocal to the square of frequency. One can neglect the ionospheric contribution at frequencies 43 GHz and above. At frequencies 10 GHz and lower, the ionospheric contribution, if not properly modeled, dominates the error budget. The solution of the problem was known for decades: to observe at two widely separated frequencies and form an ionosphere-free linear combination of observables. This approach works remarkably well at frequencies 2–10 GHz: the residual ionospheric contribution due to higher-order terms in the expansion of the dispersiveness on frequency is not detectable (Hawarey et al. 2005). Later, the systems that simultaneously record four frequencies were developed (Niell et al. 2018).

Over 90% observed sources exhibit structure detectable at images. The contribution of source structure to delay causes systematic errors. This effect was first studied in detail by Thomas (1980). When we know the source brightness distribution, we can compute the contribution to delay and correct the data. The first attempt to apply this contribution was done by Campbell et al. (1988). Although it was demonstrated by Charlot (2002) that a massive application of structure maps to correct for structure effects is feasible, and it improves results of data analysis, so far, this approach did not go beyond demonstrations, and up to now, the source structure contribution is not modeled in a routine VLBI data analysis. Plank et al. (2016) have shown through simulations that the contribution of source structure to delay at 8 GHz is in a range of 10–80 μs for *most* of the sources. Analysis of VLBI observations of 29 active galactic nuclei (AGNs) observed under MOJAVE program (Lister et al. 2016) at 15 GHz reported in Petrov & Kovalev (2017) showed results that are consistent with simulations: applying the source structure contribution from images changed positions in a range from 0.01 to 2.40 mas with the median 0.06 mas. Moór et al. (2011) presented evidence of weak correlation between jet directions and directions of observed AGN proper motion. If to scale a source image reciprocal to frequency, the contribution of source structure to delay will also be scaled reciprocal to frequency, i.e. reduced. However, one should keep in mind that it is the asymmetry of the core region at scales comparable with the resolution that affects the source structure contribution the most. This asymmetry does not vanish even at frequencies as high as 230 GHz (Kim et al. 2020) and may be more profound at high frequencies. It should also be noted that source structure changes are more significant at high frequencies.

Due to synchrotron self-absorption, the AGN core center is observed at a location where the optical depth is close to one. That location depends on frequency f . In a case when the energy of the magnetic field and relativistic particles is approximately equal (the equipartition condition), this dependence is f^{-1} (Lobanov 1998). Observations confirm that it is a common situation (Kovalev et al. 2008; Sokolovsky et al. 2011; Abellán et al. 2018), however ex-

amples of deviations of the power law from -1 are also known. When the core-shift depends on frequency as f^{-1} , the contribution to fringe phase becomes frequency independent, and since group delay is a partial derivative of phase over frequency, it does not affect group delay (Porcas 2009). At the same time, it affects fringe phase and phase delay. A detailed study of a sample of thousands AGNs, revealed that the core-shift is variable (Plavin et al. 2019), and the deviation from the equi-partition is associated with a flaring activity, typically on a time scale of several years. Therefore, in a case if a source is in the equipartition state, the core-shift does not affect absolute source positions derived from analysis of group delays, although it does affect positions derived with a method of differential astrometry based on analysis of differential phases. When the equipartition condition is violated, for instance within several years of a flare, the variable core-shift affects group delays as well, and this contribution is reciprocal to frequency.

Scintillations in the interstellar medium cause broadening of source images. As a result, the correlated flux density at long baselines is reduced. Since position accuracy is reciprocal to the projected baseline length, a drop of correlated flux density, especially if it falls below the detection limit, affects detrimentally the position accuracy. Pushkarev & Kovalev (2015); Koryukova et al. (2022) found that scattering is significant in the vicinity of the Galactic plane and in areas with a high density of the interstellar medium. This effect is reciprocal to the square of frequency and it barely affects data at 22 GHz, but it may severally affect observations at 2–8 GHz.

1.1. *Problem statement and approach*

As we see, the impact of four effects, atmospheric path delay, contribution of the ionosphere, source structure, and core-shift depends on the choice of observed frequency or frequencies. What are trade-offs? One can consider two extreme cases: 1) a frequency-dependent bias in position estimates is unique to each band and has to be measured; 2) the frequency-dependent bias is negligible. Realistically, we can assume the truth is between these extremes, but is it close to case 1 or to case 2? An answer to this question has a profound impact on strategy of radioastrometry.

If the frequency-dependent bias is significant, then a celestial reference frame to each frequency band or each combination of frequency bands needs be constructed. This would require significant resources that have to be taken by displacing other projects. From the other hand, if the frequency-dependent bias is negligible, then the radio celestial reference frame is frequency independent as well, and we can combine observations at different frequencies to improve the position accuracy.

Let us summarize five sources of frequency-dependent systematic errors:

- Impact of path delay in the neutral atmosphere: disfavors frequencies above 20 GHz since at higher frequencies observations at low elevations are down-weighted or lost due to high atmospheric opacity;
- impact of path delay in the ionosphere: disfavors single-band observations below 43 GHz;
- impact of the source structure: favors higher frequencies with reservations;
- impact of the core-shift: favors higher frequencies since the core-shift is reduced with frequency.
- impact of the interstellar medium: favors high frequencies;

It should be also noted that at higher frequencies in general, sources are weaker, sensitivity of radiotelescopes is lower, and therefore, precision of group delays is worse.

Had we had a precise and reliable model of the error budget of all these contributions, we could solve this problem analytically. Although there is a certain progress in this direction, we are still far from claiming that we do quantitatively understand the error budget theoretically. Therefore, I consider another approach: processing existing multi-frequency VLBI data suitable for absolute astrometry analysis and assessing differences in source position estimates. Analysis of the magnitude of frequency-dependent position biases will help us to answer the questions formulated at the beginning of this subsection: what are the trade-offs in the frequency selection for absolute astrometry programs, when should we

process observations at different frequencies combined, when should we process them separately, and finally, whether efforts for constructing celestial reference frames for each individual frequency or a frequency combination are justified by evidence.

2. OBSERVATIONS AND DATA ANALYSIS

I have processed seven VLBI datasets. They include 1) a 48 h campaign of observations with frequency switching between 2.2/8.4 GHz and 4.1/7.4 GHz with Very Long Baseline Array (VLBA); 2) a campaign of 281 experiments at 4.1/7.4 GHz with VLBA; 3) a campaign of 270 experiments at 2.2/8.4 GHz with VLBA; 4) a campaign of 2259 experiments at 2.2/8.4 GHz run by the International VLBI Service for geometry and astrometry (IVS); 5) a campaign of 153 experiments at 3.0/5.2/6.4/10.2 GHz at the network of IVS stations equipped with quad-band receivers; 6) a campaign of 90 experiments with VLBA at 23 GHz; and 7) a campaign of 8 experiments with VLBA at 43 GHz.

The original records of voltage from radio telescope receivers were correlated, and time series of cross- and auto- correlation data have been computed forming so-called Level 1 data (Deller et al. 2007, 2011). Then group delays were evaluated from cross- and auto- correlation data using the fringe-fitting procedure, with either *PLMA* (Petrov et al. 2011) or *Fourfit* software¹. I ran the fringe fitting data analysis using *PLMA* for all the data, except IVS campaigns. For the latter two campaigns I used group delays derived by *Fourfit* and stored in geodetic database files that are available at the NASA CDDIS data archive².

Further astrometric data analysis was performed using group delays. That involved several steps: computation of theoretical path delays and forming small differences between observed and modeled delays; preprocessing that includes outliers elimination, weight update, and identifying clock breaks; and parameter estimation with least squares using all the data of each observing campaign.

2.1. Data reduction and parameter estimation

I processed the data with the state-of-the-art theoretical model used in prior works, for instance in Petrov et al. (2011); Petrov (2021). In general, it follows the so-called IERS Conventions (Petit & Luzum 2010), with a number of improvements. Of them, the following are relevant for the present study: Galactic aberration was accounted for, a priori slant path delays were computed by a direct integration of equations of wave propagation through the heterogeneous atmosphere (Petrov 2015) using the output of NASA numerical weather model GEOS-FPIT (Rienecker et al. 2018), and the ionospheric contribution computed from the GNSS global ionospheric model CODE (Schaer 1999) for processing single-band delays with three important modifications: the nominal height of the ionosphere was increased by 56.7 km, elevation for the ionospheric mapping function was scaled by 0.9782, and the total electron contents was scaled by 0.85. A thorough discussion of the impact of these modifications is given in Petrov (2023).

Group delays or ionosphere-linear combinations of observables at two or more bands were fitted to the parametric model using least squares. The parameters were partitioned into three classes: global parameters that were estimated using the entire dataset, local parameters that were estimated for each observing session, and segmented parameters that were estimated for each station for an interval of time that is shorter than an observing session. The parametric model included estimation of the following global parameters: right ascensions and declinations of all the sources, station positions at the reference epoch, station velocities, sine and cosine components of harmonic site position variations (Petrov & Ma 2003), and the non-linear motion of some stations with breaks due to seismic activity modeled with B-splines with multiple knots at epochs of seismic events. Polar motion, UT1, their rate of change, as well as nutation daily offsets were estimated as local parameters. Clock function, atmospheric path delay, and the tilt of the symmetry axis of the refractivity field for all the stations were modeled as an expansion over the B-spline basis of the 1st degree. These coefficients were estimated as segmented parameters. The span between knots was 60 minutes for clock function, 20 minutes for the atmospheric path delay in zenith direction, and

¹ <https://www.haystack.mit.edu/haystack-observatory-postprocessing-system-hops/>

² <https://cddis.nasa.gov>

6 hours for tilt angles. No-net-rotation constraints were imposed on a subset of source position estimates in order to find a solution of a linear problem of the incomplete rank (see Petrov (2021) for more details). The subset of sources used for constraints included all the sources from the ICRF1 catalogue (Ma et al. 1998) that had at least 200 usable observations in processed campaigns.

2.2. Error analysis

The source position uncertainties were derived from the uncertainties of group delays following the law of error propagation. An uncertainty of group delay is computed based in the signal to noise ratio of fringe amplitude. The noise of fringe visibilities is determined by Fourfit and *PLIMA* differently. Fourfit computes the noise theoretically from the number of recorded bits. *PLIMA* uses a more sophisticated algorithm: it computes the noise level from the visibility data themselves. At the final stages of the fringe fitting procedure, the least square adjustment, *PLIMA* applies the additive reweighting procedure: it finds additive phase weight corrections for each observation that, being added in quadrature, makes the ratio of the weighted sum of residual phases to their mathematical expectations close to unity.

A similar procedure was performed for an update of group delay uncertainties. The extra variance was computed for each baseline and each experiment during a preprocessing stage of data analysis. This variance was added in

quadrature to the reported group delay uncertainties, and these inflated group delay uncertainties were used as reciprocal weights. The ratios of the weighted sum of group delay residuals to their mathematical expectations were made to be close to unity for each baseline and each experiment. The algorithm for additive variance computation can be found in Petrov (2021).

To assess the validity of reported uncertainties, I ran two additional decimation solutions for each dataset. Observations of each source were sorted in the chronological order and split into segments of 32 observations. Observations were marked as belonging to odd or even segments oooooo eeeeeee oooooo ..., where letters o and e denote odd and even segments respectively. Odd segments were downweighted by a factor of 1000 in the first decimation solution, and even segments were downweighted in the second solution. Then the estimates of source positions from odd and even decimation solutions have been compared. I computed arc lengths between position estimates and uncertainties of these arcs assuming the source position estimates are independent. First, I converted uncertainties of source positions over right ascension σ_α , over declination σ_δ , and correlations between these uncertainties to the semi-major σ_{maj} and semi-minor axes σ_{min} of the error ellipse and the position angles θ of the semi-major axes counted from the North celestial pole counter-clockwise:

$$\begin{aligned} \theta &= \frac{1}{2} \arctan \frac{2 \text{Corr } \sigma_\alpha \cos \delta \sigma_\delta}{\sigma_\alpha^2 \cos \delta^2 - \sigma_\delta^2} \\ \sigma_{\text{maj}}^2 &= \sigma_\alpha^2 \cos \delta^2 + \sigma_\delta^2 + \sqrt{(\sigma_\alpha^2 \cos \delta^2 - \sigma_\delta^2)^2 + 4 (\text{Corr } \sigma_\alpha \cos \delta \sigma_\delta)^2} / 2 \\ \sigma_{\text{min}}^2 &= \sigma_\alpha^2 \cos \delta^2 + \sigma_\delta^2 - \sqrt{(\sigma_\alpha^2 \cos \delta^2 - \sigma_\delta^2)^2 + 4 (\text{Corr } \sigma_\alpha \cos \delta \sigma_\delta)^2} / 2 \end{aligned} \quad (1)$$

Then the uncertainty of an arc between position 1 and position 2 is

$$\sigma_a^2 = \frac{1 + \tan^2(\theta_1 - \phi)}{1 + \frac{\sigma_{1,\text{maj}}^2}{\sigma_{1,\text{min}}^2} \tan^2(\theta_1 - \phi)} \sigma_{1,\text{maj}}^2 + \frac{1 + \tan^2(\theta_2 - \phi)}{1 + \frac{\sigma_{2,\text{maj}}^2}{\sigma_{2,\text{min}}^2} \tan^2(\theta_2 - \phi)} \sigma_{2,\text{maj}}^2, \quad (2)$$

where $\phi = \arctan \frac{\Delta \delta}{\Delta \alpha \cos \delta}$.

Second, I computed the histograms of the ratios of arc lengths between positions estimates

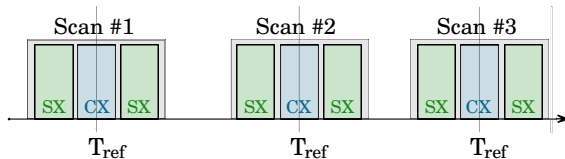


Figure 1. Data were recorded three times for every scan during BP175 campaign when antennas were on source: first at SX, then at at CX, and then again at SX.

to the arc length uncertainties — the so-called normalized arc lengths. If position uncertainties are correct, the distribution of normalized arc lengths should be Rayleighian with $\sigma = 1$. Third, I performed a multiplicative fitting of the uncertainties to the Rayleigh distribution. I considered that the position uncertainties from both odd and even decimation solutions are to be scaled by a common factor R and sought such a factor that minimizes the sum of squares of the differences of the normalized histogram and the Rayleigh distribution. When $R > 1$, the errors are underestimated. When $R < 1$, the errors are overestimated. I have rescaled position uncertainties by dividing them by \sqrt{R} in further analysis.

2.3. *Quasi-simultaneous observations at 2.2/8.4 GHz and 4.1/7.4 GHz with VLBA*

In order to assess the impact of a frequency change of dual-band observations on source position estimates, a special 48 hr campaign BP175 was observed with VLBA. The campaign was split into ten blocks of 3 to 8 hours long. Data from each pointing was recorded three times: first at 2.2/8.4 GHz (SX bands), then the receiver was changed to 4.1/7.4 GHz (CX), and then back to SX (see Figure 1). More detail of this campaign can be found in (Petrov 2021). In total, 13,512 group delays at all bands were computed at exactly the same reference epoch. SX and CX group delays were processed independently, and positions of 394 observed sources were estimated in two separate least square (LSQ) solutions.

2.4. *The geodesy and absolute astrometry VLBI campaign at 2.2/8.4 GHz with VLBA*

A program of regular twenty four hour observations with VLBA and up to 10 other stations runs since 1994 through present with a cadence

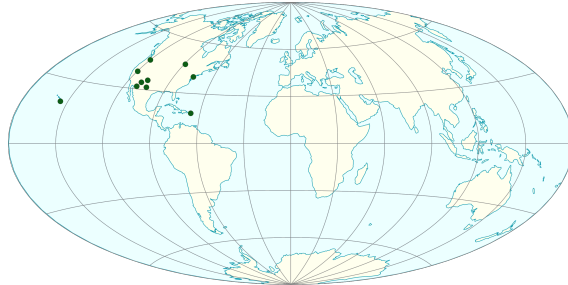


Figure 2. Location of 10 VLBA radiotelescopes.

of approximately 6 experiments per year. See the distribution of VLBA stations in Figure 2. The purpose of that program is monitoring positions of radiotelescopes and improvement of source coordinates. Observations are done at 2.2 and 8.4 GHz simultaneously with a spanned bandwidth of 140 and 496 MHz respectively. More information about this campaign can be found in Petrov et al. (2009). I included in data analysis experiments from similar geodetic programs cn18 and cn19 and three campaigns of the second epochs of VLBA Calibrator Survey: bg219, ug002, and ug003 (Gordon et al. 2016). I selected 270 experiments since April 15 1998 through November 28 2022, in total 3.4 million observations. Data from stations other than VLBA were discarded in the solutions in order to eliminate the impact of the network for comparison with other datasets that used only VLBA antennas. The R-factor from the decimation solutions is 0.94.

2.5. *The absolute astrometry VLBI campaign at 4.1/7.4 GHz with VLBA*

A program of the wide-field survey with VLBA at 4.1/7.4 GHz ran in 2013–2022 (Petrov 2021). That program targeted 29,851 sources. Most of the target sources were weak with correlated flux densities in a range of 10–100 mJy, and only one half have been detected. In addition to target sources, a number of strong sources were observed as calibrators. It is just observations of these calibrator sources that were mainly used in comparisons. I included data of 281 experiments, 0.6 million observations, under this program for data analysis. The R-factor from the decimation solutions is 1.24.

2.6. *The geodesy VLBI campaign at 2.2/8.4 GHz at the IVS network*

An on-going campaign of regular geodetic VLBI observations R1 and R4 (Thomas et al. 2024) runs two times a week on Mondays and Thursdays since 2002. There are 43 stations that joined these observations. I retained 33 stations that participated in 30 or more experiments for data analysis. See station distribution in Figure 3. In total, 6.9 million group delays from 2259 twenty-four hour experiments were used in data analysis. The R-factor from the decimation solutions is 1.13.

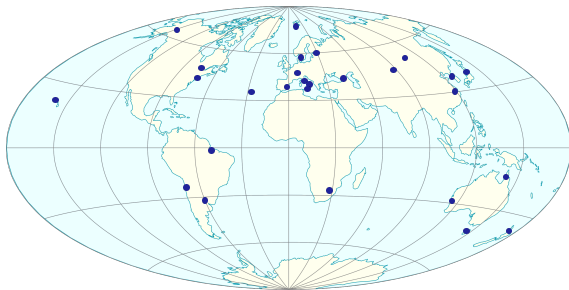


Figure 3. Location of 33 radiotelescopes that participated in IVS SX R1R4 campaigns.

2.7. *The geodesy VLBI campaign VO at 3.0/5.2/6.4/10.2 GHz at the IVS network*

Another ongoing campaign of regular geodetic VLBI observations VO (Niell et al. 2018) runs at a network of 13 twelve meter radiotelescopes 2–4 times a month since 2017. The network of stations evolved with time. The map of station distribution by the end of 2023 is shown in Figure 4. Observations are performed simultaneously at four bands 3.0, 5.2, 6.4 and 10.2 GHz. Ionosphere-free group delays are directly estimated from these data during fringe fitting. In total, 1.3 million group delays from 153 experiments were used in data analysis. The R-factor from the decimation solutions is 1.53.

2.8. *The absolute K band astrometry VLBI campaign at 23 GHz with VLBA*

A number of absolute astrometry campaigns ran with VLBA at K band (23–24 GHz) since 2002. They include VCS5 campaign (Kovalev et al. 2007), KQ-survey (Lanyi et al. 2010; Charlot et al. 2010), Kband-CRF (de Witt et al. 2023a), BJ083, UD001, UD009 (Krasna et al. 2023), and UD015 campaigns. The recorded bandwidth varied from 32 MHz at

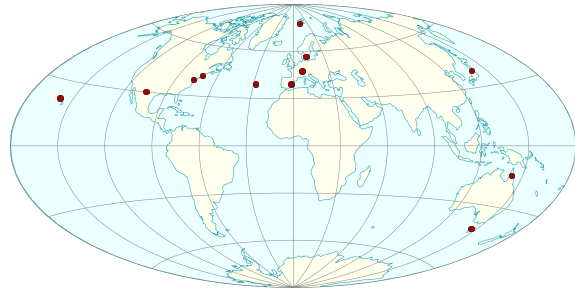


Figure 4. Location of 13 radiotelescopes that participated in the IVS quad-band campaign.

single right circular polarization in early experiments to 512 MHz, dual polarization in 19 latest observing sessions. In total, 99 experiments, 1.5 million group delays were used in data analysis. Of 1298 observed radio sources, 1126 have been detected. The R-factor from the decimation solutions is 0.92.

2.9. *The absolute Q-band astrometry VLBI campaign at 43 GHz with VLBA*

There were two VLBA absolute astrometry observing campaigns at Q-band (43 GHz) with VLBA: KQ-survey in 2002–2003 and UD014 in 2021. These campaigns targeted mainly the strongest sources. In total, 72,498 group delays from 8 experiments were used in data analysis. Of 525 observed sources, 504 have been detected. The R-factor from the decimation solutions is 1.17.

3. ANALYSIS OF THE DIFFERENCES IN SOURCE POSITION DERIVED FROM SEVEN DATASETS

I estimated source positions using each dataset. Then I formed the differences in positions of those sources that were observed and have been detected in both campaigns and which positions were derived with a sufficient accuracy in order to investigate small differences. I used two criteria to select common sources for the statistical study: the number of observations used in solutions and the position uncertainty. I normalized residuals by dividing them by reweighted uncertainties. In order to mitigate the impact of outliers on the source statistics, I performed an iterative procedure of outlier elimination. I retained for further analysis only the sources with normalized residuals by module less than some number, by default 5.

3.1. Comparison of source positions at 4.1/7.4 GHz vs 2.2/8.4 GHz

Comparison of quasi-simultaneous 2.2/8.4 versus 4.1/7.4 GHz did not reveal a systematic a pattern. The rms difference was 0.54 mas over declination and 0.56 mas over right ascension scaled by $\cos \delta$. It should be noted that that campaign was a pilot study of a large observing program focused on observations of weak sources. This explains relatively large position uncertainties and differences in position estimates.

Processing a significantly larger dataset of non-simultaneous 2.2/8.4 GHz and 4.1/7.4 GHz observations from the VLBA network allowed me to lower the limit of position differences. Plots of differences are featherless — see Figures 5–6; the biases in right ascension and declination are 0.004 and 0.028 mas respectively, and the rms of the differences is 0.27 and 0.39 mas over right ascension and declination among 734 common sources with formal uncertainties greater than 0.5 mas.

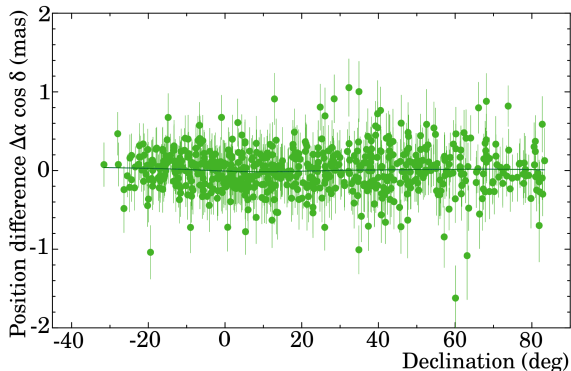


Figure 5. The differences in right ascension scaled by $\cos \delta$ factor derived from analysis of 2.2/8.4 and 4.1/7.4 GHz VLBA observations.

The histogram of normalized arc lengths between position estimates computed using the original uncertainties displays a significant deviation from the Rayleigh distribution (Figure 7). I computed a series of histograms of normalized differences in right ascension scaled by $\cos \delta$ and declination with different variances that were added in quadrature to position uncertainties. I found the variances that provided the minimum of the rms differences between a histogram and the Gaussian distributions. These variances are 0.11 and 0.09 mas over right ascension and declination respec-

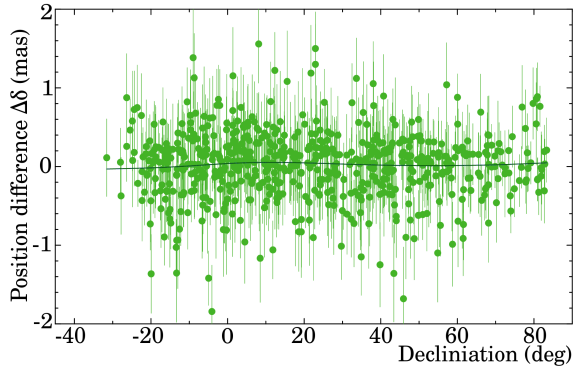


Figure 6. The differences in declination derived from analysis of 2.2/8.4 and 4.1/7.4 GHz VLBA observations.

tively. The distribution of the normalized arc lengths became much closer to the Rayleigh distribution after inflating the uncertainties.

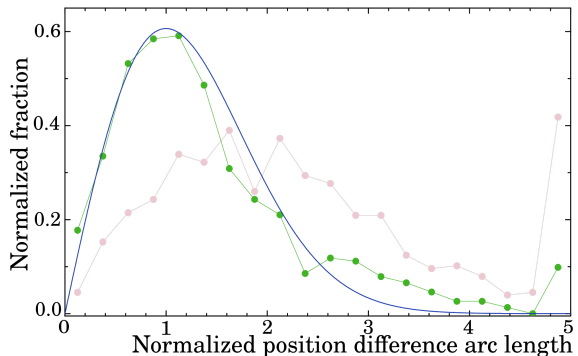


Figure 7. The differences in normalized arc lengths between source source positions derived from analysis of 2.2/8.4 and 4.1/7.4 GHz VLBA observations. Pale pink points show the histogram computed with original uncertainties and green points show the show the histogram computed with inflated uncertainties.

3.2. Comparison of source positions from quad-band observations versus positions from 2.2/8.4 GHz IVS observations.

VLBI observing program at 3.0/5.2/6.4/10.2 GHz with the so-called VLBI Global Observing System (VGOS) network dedicated to determination of the Earth orientation parameters and station positions intensively used a short list of sources. There are 204 sources with 32 or more good observations common among other programs. Plots of the differences are shown in Figures 8–9. There are two outliers in right ascension differences, but otherwise, the plots do not exhibit systematic patterns.

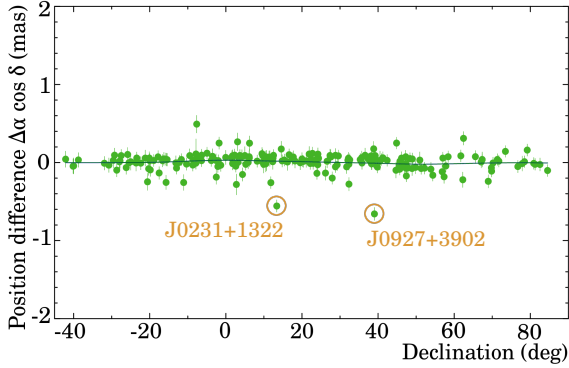


Figure 8. The differences in right ascension scaled by $\cos \delta$ factor derived from analysis of 3.0/5.2/6.4/10.2 and 2.2/8.4 GHz geodetic VLBI observations.

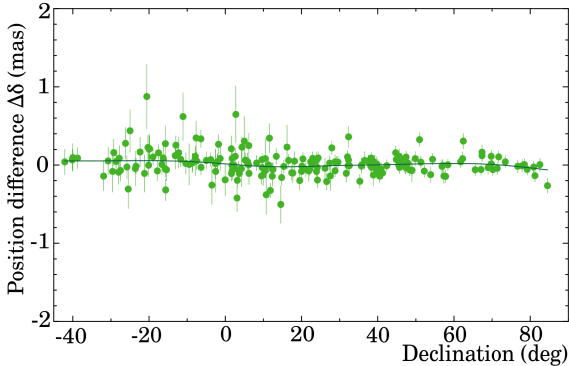


Figure 9. The differences in declination derived from analysis of 3.0/5.2/6.4/10.2 and 2.2/8.4 GHz geodetic VLBI observations.

In a similar way, as we saw in the prior comparison, the histogram of normalized arc lengths does not agree with the Rayleigh distribution despite of scaling VGOS position uncertainties by the factor of 1.53 derived from the decimation test. I found that the uncertainties over right ascension and declination should be inflated by adding in quadrature 0.070 and 0.086 mas respectively to fit their normalized histogram to the Gaussian distribution. Biases in right ascension and declination are 0.006 and 0.007 mas respectively. The rms of position differences over right ascension and declination are 0.09 and 0.13 mas respectively.

3.3. Comparison of source positions from 2.2/8.4 GHz at the IVS and VLBA networks.

It is instructive to extend analysis of position differences determined from observations at the same network and different frequencies,

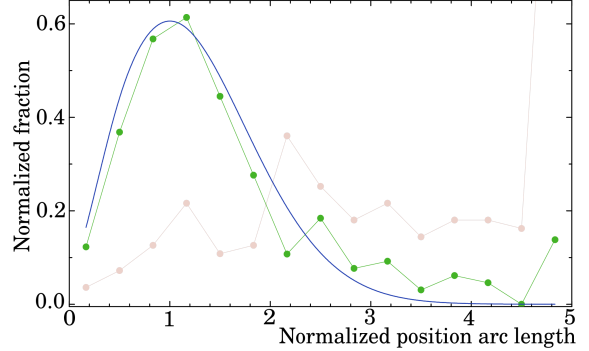


Figure 10. The differences in normalized arc lengths between position estimates derived from analysis of 3.0/5.2/6.4/10.2 and 2.2/8.4 GHz geodetic VLBI observations. Pale pink points show the histogram computed with original uncertainties and green points show the histogram computed with inflated uncertainties.

to the differences derived from observation at different networks and at the same frequencies. This analysis allows us to assess the magnitude of frequency dependent systematic errors with respect to frequency independent errors. Plots of differences in position estimates of 665 common sources with formal uncertainties less than 0.5 mas and at least 32 good observations are shown in Figure 11–12. We see a number of outliers and a small declination bias at low declinations. The overall bias in right ascension is 0.004 mas and 0.074 mas in declination.

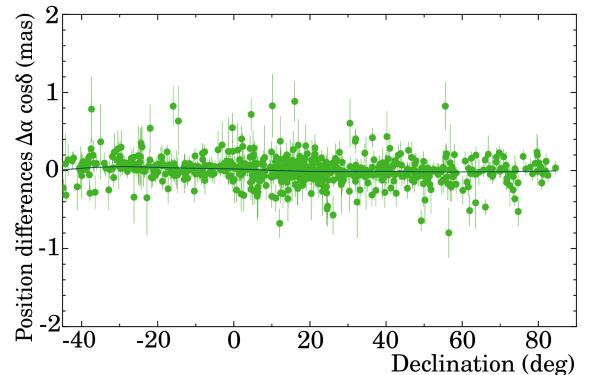


Figure 11. The differences in right ascension scaled by $\cos \delta$ factor derived from analysis of 2.2/8.4 GHz observations at VLBA and R1R4 networks.

Fitting the normalized position differences to the Gaussian distribution, I found that the uncertainties over right ascension and declination should be inflated by adding in quadrature 0.060 and 0.087 mas respectively to provide

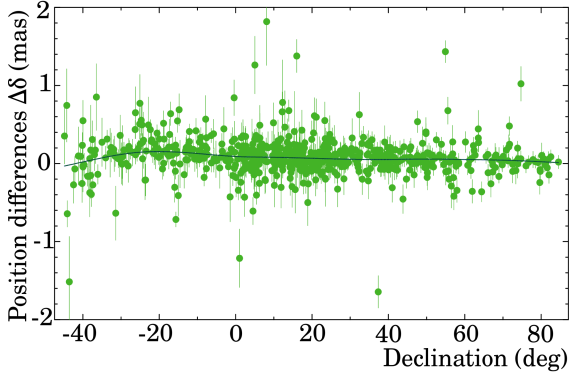


Figure 12. The differences in declination derived from analysis of 2.2/8.4 GHz observations at VLBA and R1R4 networks.

the best fit. These parameters are remarkably close to those found in the comparison between VGOS and VLBA observations. The rms of the differences in right ascension and declination are 0.090 and 0.138 mas respectively.

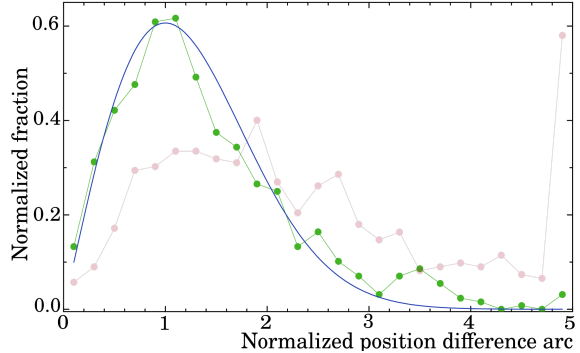


Figure 13. The differences in normalized arc lengths between source positions derived from analysis of 2.2/8.4 GHz data from VLBA and R1R4 networks. Pale pink points show the histogram computed with original uncertainties and green points show the the histogram computed with inflated uncertainties.

For completeness, I analyzed the differences between source position estimates derived from VGOS and VLBA SX data. The declination bias was -0.056 mas, the extra noise in right ascension and declination was 0.071 and 0.064 mas respectively. The rms of the differences in right ascensions and declination are 0.098 and 0.138 mas respectively. This triple comparison helped to identify the source catalogue that has a declination bias with respect to other catalogues: VLBA SX.

When we consider the difference between two source position catalogue, in general, we cannot tell what is the contribution to these differences of each individual catalogue. However, when differences of *three* catalogues of the same sources are available, we can do it using the so-called three corner hat method (Gray & Allan 1974). Considering that the intrinsic errors in catalogues c_1, c_2, c_3 do not have correlations between each others, we can write

$$\begin{aligned} \text{Var}(c_1 - c_2) &= \text{Var}(c_1) + \text{Var}(c_2) \\ \text{Var}(c_1 - c_3) &= \text{Var}(c_1) + \text{Var}(c_3). \\ \text{Var}(c_2 - c_3) &= \text{Var}(c_2) + \text{Var}(c_3) \end{aligned} \quad (3)$$

Solving equation 3, we get

$$\begin{aligned} \text{Var}(c_1) &= \frac{1}{2}(\text{Var}(c_1 - c_2) + \text{Var}(c_1 - c_3) - \text{Var}(c_2 - c_3)) \\ \text{Var}(c_2) &= \frac{1}{2}(\text{Var}(c_2 - c_3) + \text{Var}(c_1 - c_2) - \text{Var}(c_1 - c_3)). \\ \text{Var}(c_3) &= \frac{1}{2}(\text{Var}(c_1 - c_3) + \text{Var}(c_2 - c_3) - \text{Var}(c_1 - c_2)) \end{aligned} \quad (4)$$

Table 1. The intrinsic (columns 2 and 3) and formal errors (columns 4 and 5) of source positions catalogues from VLBA, VGOS, and R1R4 catalogues in mas. $\cos \delta$ factor is applied to errors in right ascension.

	$\sigma_\alpha(i)$	$\sigma_\delta(i)$	$\sigma_\alpha(f)$	$\sigma_\delta(f)$
R1R4 SX	0.05	0.06	0.01	0.03
VGOS quad-band	0.10	0.05	0.02	0.04
VLBA SX	0.05	0.07	0.02	0.03

This method allows us to solve for intrinsic errors of each catalogue. Here I used 197 sources common in all three catalogues. The result is presented in table 1. We see that the intrinsic errors of individual catalogues are at a level of 0.05–0.07 mas in right ascension and declination, except the SX VLBA catalogue that has intrinsic errors in right ascension at a level of 0.11 mas. The median formal uncertainties scaled by a factor of R from the decimation test are shown as well for comparison.

3.4. Comparison of K band positions against SX positions

There are in total 1007 common radio sources that have been detected in both VLBA datasets at 23 GHz and 2/8 GHz. I used in further analysis 858 sources that had at least 32 common observations in both datasets, position uncertainties < 0.5 mas over declination or right ascension scaled by $\cos \delta$, and normalized residuals less than 7.

The position differences in right ascension scaled by $\cos \delta$ factors as a function of declination are shown in Figures 14–15. The solid lines are the boxcar averages. Table 2 summarizes the statistics of the sample. While the plot of differences in right ascension is featureless, except some outliers, the plot of differences in declination shows a systematic pattern: the declination uncertainties of the sources in the Southern Hemisphere are noticeably larger and their scatter is greater.

Observations of southern sources with the VLBA array situated in the Northern Hemisphere are made in a disadvantageous configuration compared with observations of northern sources. These sources usually cannot be seen at all the baselines, and the lower declination of a given source, the less stations can simultaneously see it. Since two the southmost VLBA stations, MK-VLBA in Big Hawaiian is-

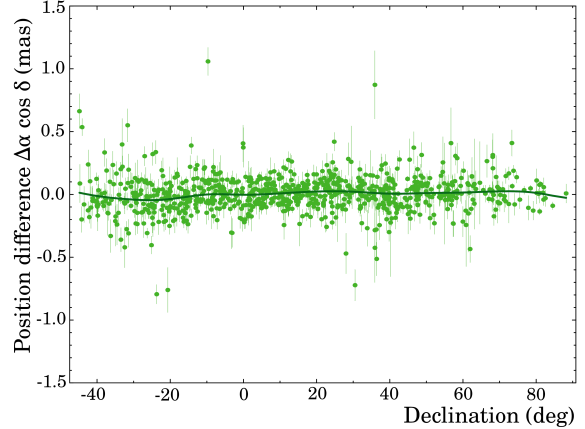


Figure 14. The differences in right ascension scaled by $\cos \delta$ from analysis of VLBA data at 2.2/8.4 GHz versus 23 GHz.

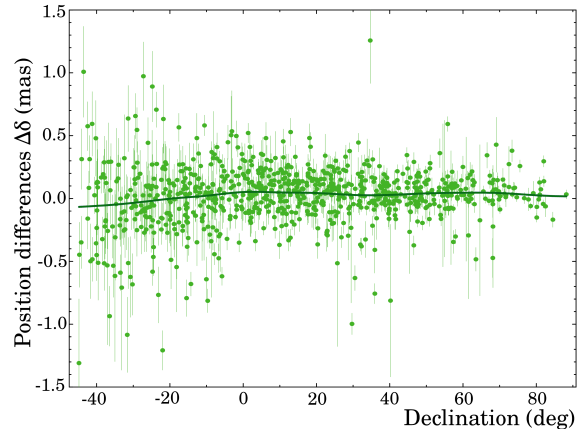


Figure 15. the differences in declination from analysis of VLBA data at 2.2/8.4 GHz versus 23 GHz.

Table 2. Statistics of positions uncertainties of source position from SX and K band VLBA observations in mas.

	SX	K	Diff
RA $\cos \delta$ median	0.051	0.036	
Dec median	0.085	0.061	
RA $\cos \delta$ bias			0.002
RA $\cos \delta$ rms			0.109
Dec bias			0.033
Dec rms			0.156
Arc median			0.152

land and SC-VLBA in St. Croix island in the Caribbean sea have also the widest spread in longitude, southern sources are often observed at a sub-network with a long equatorial baseline vector projection and a short polar baseline

vector projection. This explains a disparity in position uncertainties between declination and right ascension. However, a more detailed analysis reveals that the declination dependence of differences in declination is stronger than the declination dependence of uncertainties. This indicates there is another factor that affects the differences beyond a purely geometric effect.

I split the dataset into seven segments over declinations and computed statistics within each segment. In Figure 16 blue hollow circles show the median 23 GHz position uncertainties and green solid circles show median differences in declination. Both statistics grow with declination, but the position differences grow faster with a decrease in declination. Petrov (2023) investigated the impact of residual ionospheric errors on source positions after applying the contributions derived from the GNSS global ionospheric model. I showed in that paper that the residual contribution causes a declination dependent extra noise in source positions derived from processing data at VLBA. The origin of this declination dependence is the latitude dependence of the electron contents in the ionosphere: the total electron contents in the equatorial bulge is up to one order of magnitude higher than in the polar regions. Since observations of low declination sources at the northern arrays such as VLBA have to be done mainly in the southern directions where the total electron contents is systematically higher, the residual ionospheric path delay contribution is systematically higher with respect to observations of high declination sources. The pink thick line in Figure 16 shows the K band extra variance in declination (Figure 14 in Petrov (2023)) derived from the comparison of the ionospheric path delay from dual-band SX VLBA observations and path delay from the GNSS ionospheric model and then scaled by the square of the frequency ratio $(23.7/8.6)^2 = 7.6$. We see that the observed growth of differences in declination with declination is in a reasonable agreement with that model. It should be stressed that the model of the increased errors in declination was derived without any knowledge of K band astrometry, and therefore, can be considered as an independent source of information.

Inspired by the agreement of the model with observations, I decided to investigate the dif-

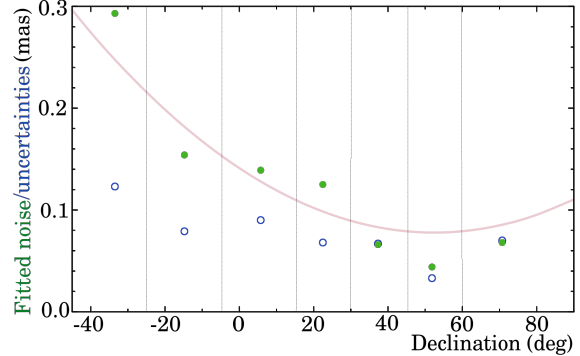


Figure 16. Green solid circles show position differences in declination from analysis of VLBA data at 2.2/8.4 GHz versus 23 GHz at 7 declination segments. Blue hollow circles show the median K band position uncertainty. The pink solid line shows a predicted additional variances in declination due to residual errors in the ionospheric contribution to path delay (Petrov 2023).

ferences in astrometric positions further and attempted to solve an ambitious problem: to build a *quantitative* stochastic model of the differences. Figure 17 shows the normalized histogram of normalized arc lengths between K band and SX source position estimates. If there were no systematic errors, and the reported uncertainties were correct, the distribution should have been Rayleighian with $\sigma = 1$ (blue thick line in Figure 17). We see significant discrepancies. Then I added in quadrature the extra noise in source positions due to mismodeling the ionospheric contribution to group delay shown in Figure 14 of Petrov (2023) to the K band source position uncertainties. Specifically, I used the following regression:

$$\begin{aligned}\sigma_\alpha &= a_\alpha + b_\alpha (\delta - c_\alpha) + d_\alpha / (\delta - e_\alpha) \\ \sigma_\delta &= a_\delta + b_\delta (\delta - c_\delta) + d_\delta (\delta - e_\delta)^2,\end{aligned}\quad (5)$$

where $a_\alpha = 0.060$ mas, $b_\alpha = 0.000011$ mas, $c_\alpha = 10^\circ$, $d_\alpha = 1$ mas, $e_\alpha = 110^\circ$; $a_\delta = 0.090$ mas, $b_\delta = 0.000350$ mas, $c_\delta = 90^\circ$, $d_\delta = 0.000023$ mas, $e_\delta = 60^\circ$.

The distribution of normalized arc lengths with modified uncertainties that accounts for the contribution of the residual ionosphere on source positions is shown with pink pale circles in Figure 17. The disagreement with the Raleigh distribution is substantially reduced, but not eliminated. That means there is another unaccounted sources of differences in source positions.

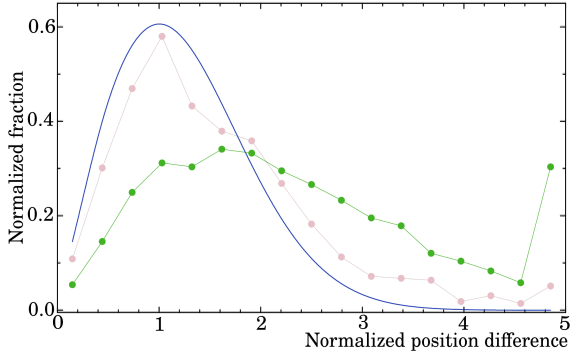


Figure 17. The distribution of normalized arc lengths between K band and SX position estimates. Green bright circles show the distribution using original data. Pale pink circles show the distribution with the contribution of the residual ionospheric noise applied. The thick blue line shows the Rayleigh distribution with $\sigma = 1$ as a reference.

Let us recollect that the position differences have two components. They can be characterized as an arc and a position angle counted counter-clockwise from the declination axis. Figure 18 shows the normalized distribution of these position angles. In the absence of systematic errors, that histogram would have been flat (see the thin red dashed line). But the histogram shows two broad peaks along the declination axis, which is a manifestation of systematic errors. That means the position differences along the declination axis are more prevailing. The disparity in the peak amplitudes means there is a declination bias, and since the peak along 180° is greater than the peak along 0° , the bias is positive.

I fitted the empirical distribution with a simple model that consists of a constant and a sum of two Gaussians. The maxima are at -1° and 183° respectively. The second moments of the Gaussians turned out to be very close: 31° and 32° .

All the sources observed in this campaigns were AGNs. Almost all AGNs exhibit morphology of a featherless core and a jet milliarcsecond scales. I re-drew the histogram counting the position angle from jet directions. The jet directions were determined for all the sources used in this investigation by Plavin et al. (2022). The histogram shows two broad peaks at -1° and at 207° . Like in a case of the dependence of position angle with respect to the North celestial pole, I fitted the histogram to a similar model of two Gaussians

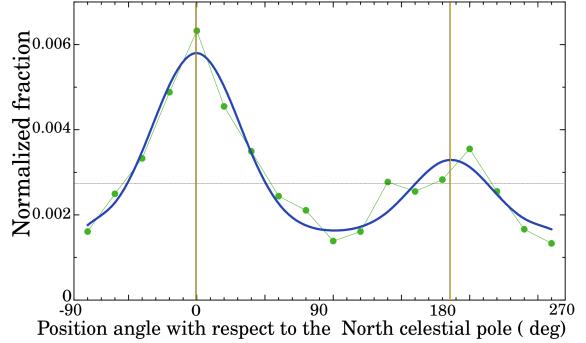


Figure 18. The normalized distribution of position angles of source coordinates derived from SX data counted from the North celestial pole relative to the source coordinates derived from the K band data solution (green circles). The solid blue line shows its fit with two Gaussians and a constant. The yellow vertical lines show the maxima. The thin dashed red line shows the uniform distribution.

and a constant term. The primary peak along jet directions is 25% higher and 10% narrower than the secondary peak in the direction opposite to the jet. The contribution of the source structure and the residual core-shift due to a violation of the equi-partition condition would cause a position offset along the jet. These contributions are frequency dependent, and they were expected to emerge on a position angle histogram when position estimates from observations at different frequencies are compared. However, the magnitude of this effect was not known.

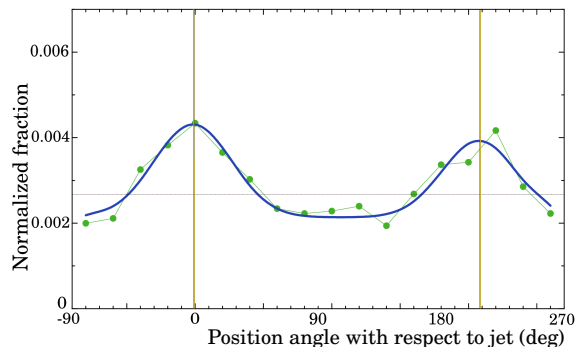


Figure 19. The normalized distribution of position angles of source coordinates derived from SX data counted from jet directions relative to the source coordinates derived from the K band data solution (green circles). The solid blue line shows its fit with two Gaussians and a constant. The yellow vertical lines show the maxima. The thin dashed red line shows the uniform distribution.

With some extra efforts we can infer the magnitude of the extra noise along jet directions from the histogram themselves. To perform a quantitative estimate and assess an uncertainty of that estimate, I performed a Monte Carlo simulation.

I generated a random sequence of the simulated SX versus K band position differences in a form of a sum of two terms: $R_o + R_i$. The first term is the observation noise. This term is the difference of two 2D Gaussian processes with the zero first moment and known second moments. These second moments were set to uncertainties in right ascension and declination as well as their correlations for each source from the compared catalogues. R_i is a 2D Gaussian process with components along declination $A_i \cos a_i$ and along right ascension $A_i \sin a_i$, where $A_i = G(s_i, \sigma_{A_i})$ and $a_i = G(0, \sigma_{am})$. Here $G(a, b)$ denotes the Gaussian function with the first and second moments a and b respectively. This process is supposed to model the extra noise in source position due to the contribution of the residual ionospheric path delay. I fixed the second moment of the noise in angles σ_{am} to the value that fit histograms Figures 18: 30° . I varied s_i and σ_{A_i} on a two-dimensional grid and sought for those s_i and σ_{A_i} , that provide the best fit to the modeled histogram in Figures 18 shown with the solid blue line. I ran 1024 trials in the inner loop. Then I ran the outer loop 64 times with a different seed of the random number generator. I got the time series of s_i and σ_{A_i} and computed their mean and root mean square.

I ran a similar procedure for accounting an extra noise along jet directions. The position differences were represented as $R_o + R_j$. The second term R_j is the 2D Gaussian process with components along declination $A_j \cos(a_j + j)$ and along right ascension $A_j \sin(a_j + j)$, where j is a jet direction. I fit this stochastic model to the modeled histogram in Figure 19. I ran this procedure two times, once with the original histogram and the second time with the modified histogram: I changed the position of the second maximum from 207° to 180° . The location of the second maximum at 207° does not fit a simple model of the Gaussian noise along jet directions. The cause of the secondary maximum shift is unclear. The use of the Gaussian noise along jet directions to represent a histogram that has a secondary peak

Table 3. Estimates of the bias of the ionospheric noise (upper row) and the noise along jet directions from fitting the position angle histograms in mas.

	bias	σ
orig north	0.053 ± 0.012	0.089 ± 0.032
orig jet	0.011 ± 0.007	0.093 ± 0.027
modified jet	0.010 ± 0.007	0.121 ± 0.023

at 207° will cause an underestimation of the second moment estimate. The artificial shift of the second maxima to 180° eliminates that problem and provides a higher value of the estimate. However, since the observed histogram has the secondary maxima at a different location, that value of the second maxima will be an overestimation. Therefore, these two estimates provide the upper and lower limits. It should be noted that since the distribution of jet directions is uniform, the source position noise driven by the residual ionospheric path delay and the noise along jet directions are uncorrelated. That means the ionosphere driven noise will not affect the histogram of the jet driven noise and vice versus.

Table 3 shows results of these Monte Carlo trials. Adding the contribution of the residual ionosphere to the contribution of the extra noise along the jet, we get 0.130 mas. Taking the mean uncertainty of of K and SX band position estimate differences in right ascension scaled by $\cos \delta$ (0.043 mas) and in declination (0.073 mas) and comparing them with lines 4 and 6 of Table 2, we get an excess noise 0.10 and 0.14 mas over right ascension and declination.

In addition, I use the histogram of normalized arc lengths between K band and SX band position estimates to estimate the contribution of the two origins of the excessive noise. I represented the extra noise as $\lambda_i R_i(\delta) + \lambda_j R_j(j)$, where $R_i(\delta)$ is the ionospheric noise according to the regression expression 5, and $R_j(j)$ is the same process as used for the fitting of the histogram with respect to jet directions with $s_j = 0.011$ mas and $\sigma_{A_i} = 0.093$ mas taken from Table 3. I considered λ_i and λ_j as free dimensionless admittance factors. I evaluated λ_i and λ_j from a broad range [0.2, 2.0] with a step of 0.01 to provide the best fit to the histogram of normalized arc lengths. In order to provide a rough estimate of the uncertainty of that fit, I varied the number of bins in the histogram

in a range of 15 to 25 and computed the mean and the rms of the estimates. The estimates are $\lambda_i = 1.10 \pm 0.07$ and $\lambda_i = 0.91 \pm 0.11$.

Although both approaches, fitting the histogram of position angles and fitting the histogram of normalized arc lengths, uses the same source position catalogues, these results are independent. We can consider an arc length and a position angle as two components of the position differences. Therefore, the agreement within one standard deviation of these two approaches is very encouraging. Figure 20 shows the histogram of normalized arc lengths with the extra noise due to the residual ionospheric contribution and the extra noise along jet directions applied with the admittance factors equal to unity. Compare it with Figure 17.

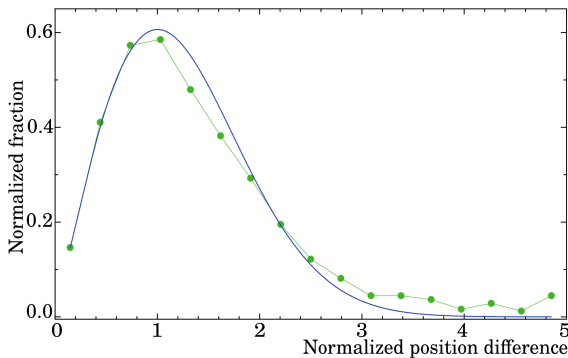


Figure 20. The distribution of normalized arc lengths between K band and SX source position estimates with the contribution from the residual ionosphere and an extra noise along jet directions applied with the admittance factors equal to one. The thick blue line shows the Rayleigh distribution with $\sigma = 1$ as a reference.

Finally, to investigate the impact of scattering in the interstellar medium, I reran the comparison by including and excluding observations with galactic latitude less than 5° . I included sources with position differences up to 1 mas in this comparison. I found that the agreement in the area within 5° of the Galactic plane is worse by 34% in right ascension and 37% in declination with respect to the area above the plane. I attribute these differences to an increase of source position errors from 2.2/8.4 GHz data with respect to positions from 23.6 GHz that are mostly not affected.

3.5. Comparison of Q band positions against SX positions

I compared source positions derived from Q-band against those derived from K band. The comparison showed a bias -0.14 mas over declination. The rms of position differences of 284 compact sources is 0.25 mas over right ascension scaled by $\cos \delta$ and 0.42 mas over declination, which is about 60% greater than median Q-band position errors after adding an extra noise in quadrature to make the errors over right ascension and declination Gaussian: 0.17 and 0.34 mas respectively.

4. DISCUSSION

Table 4 summarizes the differences in source position estimates. The first five rows show results of comparison of source position determination using dual- and quad-band VLBI observations. Comparison of positions from quad-band data versus dual-band data shows that the extra variance in positions unaccounted in reported errors is at a level of 0.07 mas. This noise does not depend on a choice of frequency bands: the use of 2.2/8.4, 4.1/7.4 or quad-band data do not introduce discernible systematic errors. Comparison of positions from CX data at 4.1/7.4 GHz shows a noticeably greater scatter, but no systematic pattern. It should be noted that CX VLBA dataset analyzed here originates from different programs that have been scheduled in a different way than all other programs in this study. Bright sources were observed as calibrators, and the schedules were not optimized to reach the highest position accuracy of calibrators. Nevertheless, the extra noise for the comparison with source positions from CX data is on par with other catalogue pairs.

Some comparisons revealed declination biases at a level comparable with the accuracy of source position catalogues. Since these biases emerged also in the comparisons of source positions derived from data at the same bands, the origin of these biases is not related to the frequency selection. It should be noted that there is no biases from source positions derived at global networks used in R1R4 and VGOS campaigns. There is a systematic bias between positions derived from the VLBA network with respect to positions derived from the global network. Mismodeling atmospheric path delay is the factor that may play a certain role.

Table 4. Statistics of the arc length differences. Column 1: the number of sources used in comparison; column 2: declination bias; column 3: rms over right ascension scaled by $\cos \delta$; column 4: rms over declination; column 5: extra noise in right ascension; column 6: extra noise in right declination; column 7: extra variance along jet directions. Units are mas.

	(1)	(2)	(3)	(4)	(5)	(6)	(7)
VLBA SX/IVS VGOS quad	204	-0.056	0.106	0.155	0.098	0.090	—
IVS R1R4 SX /IVS VGOS quad	197	0.009	0.086	0.129	0.068	0.075	—
VLBA SX/IVS R1R4 SX	665	0.061	0.125	0.153	0.060	0.091	0.111
VLBA+ SX/IVS R1R4 SX	653	0.020	0.089	0.108	0.061	0.062	0.076
VLBA CX/VLBA SX	734	0.030	0.266	0.387	0.112	0.092	—
VLBA SX/VLBA K	848	-0.042	0.126	0.182	0.082	0.107	0.093
VLBA Q/VLBA K	284	-0.160	0.245	0.170	0.300	0.426	—
IVS R1R4 SX/VLBA K	526	0.106	0.119	0.194	0.035	0.070	0.080
VLBA X/VLBA SX	4624	0.058	0.265	0.383	0.210	0.250	0.058
VLBA X/VLBA K	848	-0.040	0.191	0.256	0.083	0.128	0.088

These errors are elevation dependent. A given source is observed in a wider range of elevations at a global network. This mitigates systematic errors. To check this conjecture, I made an extended solution using SX data from VLBA, including all the stations outside the VLBA network that participated in experiments. I designated that solution as VLBA+. The declination bias dropped from 0.06 mas to 0.02 mas, and the additional noise to make the residual distribution close to the Gaussian reduced from 0.09 to 0.06 mas.

An angle of 0.07 mas, or 0.3 nrad, corresponds to 2 mm on the Earth. Geodetic VLBI experiments usually observe ~ 100 sources during 24 hr periods. If source position errors are totally uncorrelated, their impact on geodetic results will be at a level of 0.2 mm. Considering that the current accuracy of determination of the horizontal station position components is at a level of 1–3 mm from a 24 hr experiment, this is not a concern. However, the declination bias of 0.06 mas can potentially cause the latitude bias up to 2 mm. During geodetic analysis we either estimate source positions from geodetic observations or fix them to positions determined from data analysis at other networks. We should keep in mind that fixing source positions potentially may introduce systematic errors up to 2 mm.

The histograms of the position angles of source position differences with respect to jet directions showed peaks in the direction along the jet. We can identify these peaks when compare source positions from IVS R1R4 data as well — see Figures 21–22. The presence of

this pattern shows unambiguously that source structure and core shift affect source positions. Which of these two effects is dominant? The core-shift manifests as a displacement of the core with respect to the black hole. It does not depend on the network. If it were the core-shift, we would expect to see a pattern in the position angle histogram for solutions at different frequencies, 8 and 23 GHz, but not in positions derived from observations at the same frequencies. Because of the core-shift variability, we still may see the residuals of the effect in source position differences if campaign are observed in different time epochs, but the residuals are expected to be small. In contrast, source structure is network dependent. Considering that the magnitude of the noise along jet directions between SX and K band solutions at the VLBA network is comparable with the magnitude between SX solutions at the VLBA and IVS network, an explanation of the peaks at the histograms by the contribution of the unaccounted source structure is much more plausible. The magnitude of the contribution is consistent with the a priori estimate based on analysis of 15 GHz VLBA observations presented in Petrov & Kovalev (2017): 0.06 mas.

It should be noted that a dataset should be rather large in order to identify peaks in a position angle histogram. A histogram computed from 665 points with 20 bins has on average only 33 points per bin. Histograms computed using source position differences derived from VGOS datasets are too noisy to see peaks there

because on average, they have only 10 points per bin.

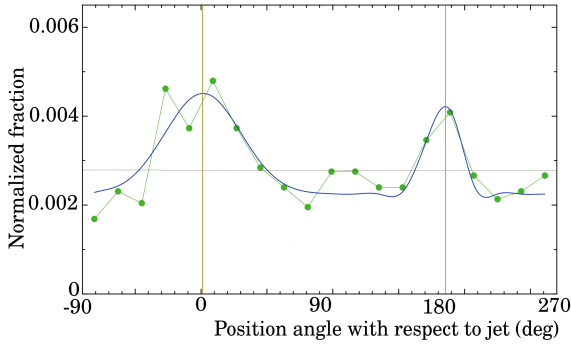


Figure 21. The normalized distribution of position angles of source coordinates derived from VLBA SX data counted from jet directions relative to source coordinates derived from IVS R1R4 SX data (green circles). The solid blue line shows its fit with two Gaussians and a constant. The yellow vertical lines show the maxima. The thin dashed red line shows the uniform distribution.

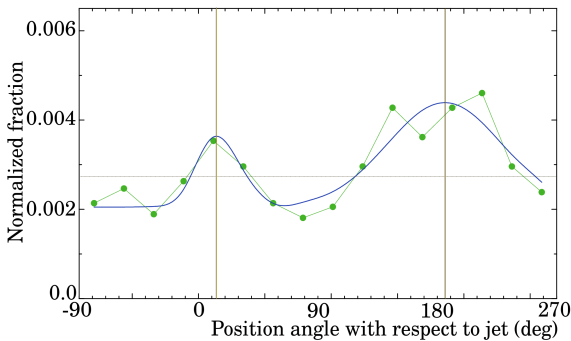


Figure 22. The normalized distribution of position angles of source coordinates derived from IVS R1R4 SX band data counted from jet directions relative to the source coordinate from VLBA K band data (green circles). The solid blue line shows its fit with two Gaussians and a constant. The yellow vertical lines show the maxima. The thin dashed red lines shows the uniform distribution.

At which frequency the impact of source structure is stronger? We can examine three hypotheses: the impact is stronger at 8 GHz, the impact is about the same, and the impact is stronger at 23 GHz. Since the contribution of the extra noise along jet directions based on the comparison of the differences in source positions derived from dual-band observations at 2.2/8.4 versus single-band observations at 23 GHz is comparable with the contribution of the extra noise from the differences in source

positions derived from observations at the same frequency, we can rule out the third hypothesis. Analysis of the position differences between 43 and 23 GHz potentially could have helped, but unfortunately, the position differences are too noisy to detect the extra noise along jet directions. We have to conclude that the presented data analysis does not allow us to discriminate two other hypotheses.

Comparison of positions of source estimates derived from single-band VLBA observations at 8 GHz against position estimates derived from dual-band observations revealed that positions have an extra noise at a level of 0.2–0.3 mas. The total differences are at a level of 0.3–0.4 mas. It should be noted that these estimates are average over several solar cycles. It is instructive to compare these estimates with the estimates of processing 5 GHz VLBA data collected during the solar minimum that had the median extra noise 0.5 mas (Petrov & Taylor 2011) and processing 8 GHz data with the Australian Long Baseline Array (LBA) — that had the extra noise of 3.2 mas (Petrov et al. 2019). The one order of magnitude difference between VLBA and LBA results is quite large. Large errors from LBA single-band observations were attributed to large errors in the ionospheric model derived from GNSS, but this explanation may need be revised considering results of the present study.

The error budget in single-band observations consists of the contribution of the frequency-independent error floor, the source structure contribution, and the ionospheric contribution. The prior analysis showed that each constituent is in a range of 0.05–0.07 mas per source position component, except the contribution of the ionosphere to the declination noise, which is greater at declination below 0° . Observed differences in source positions are fully consistent with these three constituents on a *quantitative* level, which is exciting. This analysis does not address the nature of the frequency-independent error floor. Investigation of this error floor is beyond the scope of this study and will be addressed in a separate publication.

I should stop short of declaring that these three phenomena fully explain the differences. We can establish causality if we can model a phenomenon, include it in the data reduction algorithm, and achieve a reduction of residuals.

The reduction of residuals at a level prescribed by the model establishes a necessary and sufficient criteria for the phenomena in consideration to explain the measurement results. This sets the standard of problem solving. Establishing a stochastic model described by two first moments of their distribution density allows us to establish only a sufficient condition. We can say that these three contributions are sufficient for explaining the results at the current level of accuracy, and no further phenomena are necessary to include.

Although the presence of the noise aligned with jet directions is firmly established from the analysis of the position differences, we should keep in mind that this phenomenon does not dominate the residuals. Figure 23 shows the diagram of two-dimensional differences in position estimates. The thick gray line shows the average position offset with a sector of $\pm 45^\circ$. The thin smooth red line approximates the ragged gray line with an ellipse. The thin smooth line be circular in the absence of the source structure contribution. It is just its flattening (0.2) and an offset that allows us to make an inference about the presence of the source structure contribution as a Gaussian stochastic process and to assess its first and second moments.

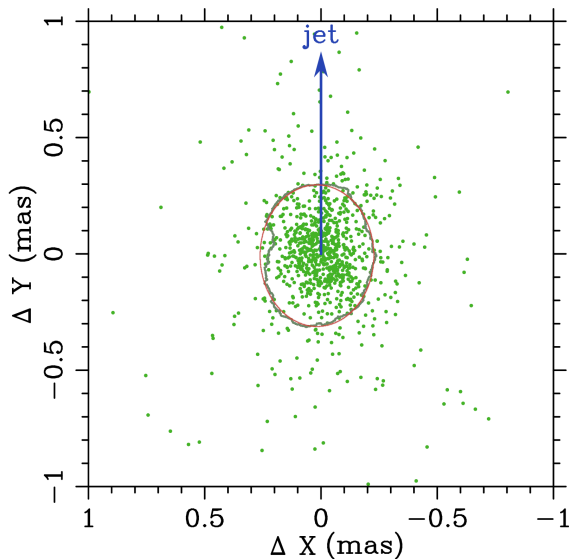


Figure 23. The differences in positions from SX band VLBA data with respect to positions from K band data. The vertical axis is aligned with jet directions. The ragged gray line shows the average position offset in a sector of 90° . The thin smooth red line shows its approximation with an ellipse.

A true stochastic model may be rather complicated. The most simple form of such a model is $\sigma^2 = R\sigma_{\text{orig}}^2 + n^2$. That form was used in the past, f.e. for deriving ICRF catalogues (Charlot et al. 2020). Even in that simplistic formulation, it is problematic to separate reliably a multiplicative factor R from an additive noise with a variance of n^2 when fitting a histogram. The distribution of the normalized arc lengths of position estimate differences from data at 23.6 and 2.2/8.4 GHz can fit reasonably well to the Rayleigh distribution either by adding in quadrature the variance or by multiplying residuals by a factor of 1.82. The use of an additive stochastic model implies that noise contributions are independent. Indeed, it is reasonable to consider that the thermal noise in receivers, the noise due to mismodeling path delay in the ionosphere, in the neutral atmosphere, and the contribution of source structure as independent, since we do not have evidence that these processes could be correlated. An explanation of appearance of multiplicative factors is problematic. The multiplicative factors can potentially explain an intrinsic measurement noise of a given source position catalogue. But in that case, we expect the same intrinsic noise to affect results in decimation tests. The decimation tests for all position catalogues, except the one derived from VGOS observations, provided the estimates of R factors close to unity, which contradicts to an assumption of the presence of a significant multiplicative factor in position uncertainties.

Figures 5,6,8,9,11,12 of source position differences had a small range to focus on the bulk of the sources. There was a number of sources that were left beyond the bounding box of the plots. The total number of outliers between dual-band, quad-band, or single-band observations exceeding 3σ was at a level of 6% and exceeding 5σ was at a level of 2%. A close examination of images usually allows us to reveal easily the cause in most of the cases. Three most common cases are shown in Figure 24. J0318+1628 with the largest offset over right ascension (-5.10 mas) with respect to the position estimate at 23.6 GHz has three compact components on its jet. An example of sources with significant position differences when observed at different frequencies was reported for the first time in Petrov et al. (2011). Later, more sources like those have

been found (for instance, Petrov 2013; Xu et al. 2022). J1217+5835 shown in the center has two brightness peaks on its image at 8.7 GHz, A and B, shown with a green cross and a red star respectively. The position estimate from 2.2/8.4 GHz corresponds to component A that is the brightest at 8.4 GHz. The 23.6 GHz image (see Figure 3 in de Witt et al. 2023b) reveals that component B is the brightest and the most compact at 23.6 GHz. The image of J1927+7358 in the right exhibits a jet. The position offset 0.6 mas along the jet is shown with a small blue arrow. This third case is less common and can be considered as a tail of the distribution of position offsets along the jet caused by unaccounted source structure.

5. SUMMARY, CONCLUSIONS, OUTCOMES, AND PERSPECTIVES

I have processed seven extended datasets that include single-band, dual-band, and quad-band observations at different frequencies and different networks, derived source positions using the absolute astrometry approach, examined their differences, and fitted a stochastic model that reconcile the normalized residuals to either the Gaussian or the Rayleigh distributions. The most important findings are the following:

1. The level of the agreement between source position estimates derived from quad-band, dual-band, and single-band observations is below a 1 nrad level, or 0.2 mas. The only systematic error found was a declination bias at a level of 0.02–0.10 mas. Since such a bias was found also in analysis of data collected at different networks, this bias is not considered to be related to a selection of observing frequencies.
2. Comparisons revealed that the number of outliers is at a level of 2 to 6% that corresponds to a normalized position difference 5σ or 3σ . The upper level of that range over normalized position differences corresponds to the sources that are definitely peculiar, the lower level corresponds to the sources that might be peculiar. Most of the peculiar sources have more than one bright component in their images.
3. The source position catalogues derived from dual-band, quad-band, and single band observations at 23.6 GHz has three constituents of the extra noise with approximately equal second moment 0.05–0.07 mas per position component. These components are 1) the intrinsic common noise, probably caused by mismodeling path delay in the neutral atmosphere; 2) the noise caused by mismodeling the ionospheric contribution when processing single-band data, and 3) the noise predominately along jet directions caused by mismodeling of source structure and possibly, by the core-shift. The latter noise manifests itself in a histogram of the position angle of the differences in source coordinate estimates with respect to jet directions in a form of two broad peaks at 0° and 180° . The astrometric analysis does not allow us to determine at which band the contribution of source structure is the greatest, but it allows us to rule out the hypothesis that source structure contribution at 23.6 GHz is greater than at 8.4 GHz.
4. The error budget of the differences between dual-band 2.2/8.4 and 23.6 GHz observations was established on a quantitative level. The source position catalogues have a common intrinsic noise level with the second moment of around 0.05 mas per component, a Gaussian noise along jet directions with the second moment of 0.09 mas that definitely affects position estimates at low frequencies and may affect position estimates at high frequencies, and the residual ionospheric noise that affects only position estimates from high frequency data. It contributes at a level of 0.07 mas to declination above 0° , grows with a decrease of declination, and reaches 0.3 mas at declination -45° . It is sufficient to consider these three phenomena in order to close the error budget.
5. Position differences derived from 2.2/8.4 and 23.6 GHz in the area of 5° the Galactic plane are 1/3 higher than otherwise. This difference is attributed to an improvement of source position accuracy at 23 GHz because observations at high fre-

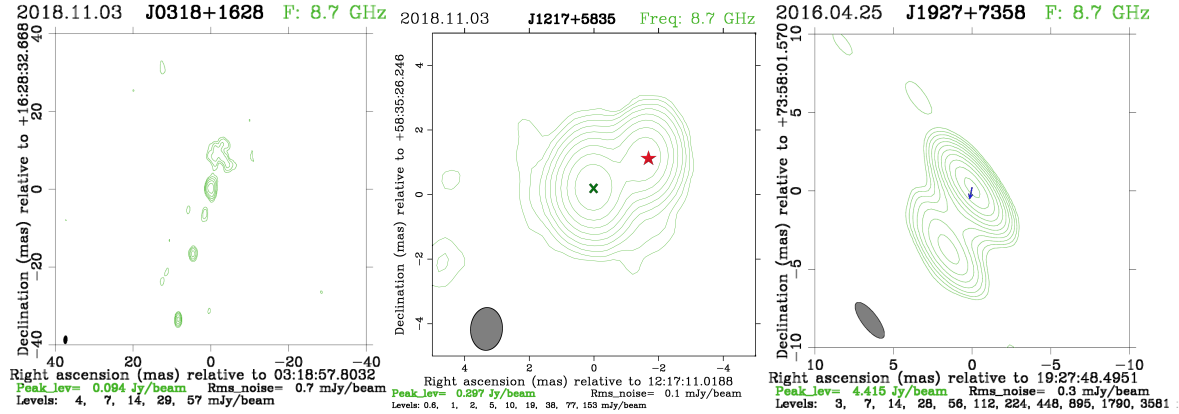


Figure 24. Image of the sources with large positions differences between coordinates derived from 8.4/2.3 GHz data with respect to coordinates derived from 23.6 GHz data. *Left:* J0318+1628 also known as CTA21 (position difference -5.10 mas in right ascension); *Center:* J1217+5835. Position estimate at 2.2/8.4 GHz is shown with a green cross, position estimate at 23.6 GHz is shown with a red star; *Right:* J1927+7358. The offset of position from 2.2/8.4 GHz data relative of its position estimate at 23.6 GHz is shown with a blue arrow. The images are taken from the Astrogeo VLBI FITS image database available at http://astrogeo.smce.nasa.gov/vlbi_images

quencies are less affected by scattering in the interstellar medium.

A frequency-dependent noise in a dual-band or quad-bands setup or in a single-band setup at 22 GHz or above affects source position estimates at a level of not exceeding 0.07 mas per component. The random noise in source positions of that magnitude affects station position estimates at a level of 0.2 mm, provided all source position estimates are uncorrelated. Source position catalogues may have declination biases up to 0.1 mas, but these biases are present in estimate of source positions not only derived from observations at different frequencies, but from observations at different networks as well, especially at networks of a small size. Expanding the network to a global scale reduces these biases to a negligible level. Possible biases in source positions derived from observations at regional networks should be checked when fixed source positions are used in data analysis.

Analysis of source positions differences suggests that observations at 23 GHz has a potential of reducing the contribution of source structure that manifests itself as the Gaussian noise along jet directions with the second moment 0.07–0.09 mas. However, the magnitude of that reduction is not yet known. At the same time, the residual ionospheric noise affects only source position estimates derived from 23 GHz data, and this noise is comparable with the extra noise due to source structure.

Presented analysis provides enough evidence to conclude that in general, absolute radio astrometry at 23 GHz currently cannot outperform astrometry at 2.2/8.4, 4.1/7.4, or 3.0/5.2/6.4/10.2 GHz. K band astrometry has a potential to outperform CX or SX astrometry only in the sky areas with high scattering, i.e. its role is rather marginal. This consideration should be taken into account for planning future observing programs.

Presented analysis provides firm evidence that a development of frequency-dependent celestial reference frame is currently not warranted. High-frequency observations in the areas with a high density of the interstellar medium may significantly improve position accuracy. Observations in these areas at 22 GHz and above are highly desirable. This is the main niche of high-frequency radioastrometry.

Since frequency-dependent source position errors, 0.05–0.07 mas per component, are comparable with common errors that affect all catalogues and with network-dependent errors, the use of dual-band, quad-band, and signal-band data at 22 GHz and above in a single least square solution will cause an additional error not exceeding 0.07 mas. This conclusion should also be taken into account for designing future astrometric programs.

Considering future perspectives, ionospheric errors can be mitigated either by observing simultaneously at 8/23 or 8/32 GHz or by solving for biases in the global ionospheric maps

derived from GNSS observations following the technique presented in Petrov (2023) with the use of data from collocated GNSS stations. If the residual ionospheric contribution will be entirely eliminated, the position accuracy can potentially be improved from a level of 0.07 mas to a 0.05 mas level.

1 This work was done using only publicly avail-
 2 able datasets 1) collected with the VLBA net-
 3 work of the NRAO and available at [https://](https://data.nrao.edu/portal/)
 4 data.nrao.edu/portal/ and 2) collected with
 5 the IVS network and available at the NASA
 6 Crustal Dynamics Data Informational System
 7 (CDDIS) [https://cddis.nasa.gov/archive/](https://cddis.nasa.gov/archive/vlbi/)
 8 [vlbi/](https://cddis.nasa.gov/archive/vlbi/). The NRAO is a facility of the Na-
 9 tional Science Foundation operated under co-
 10 operative agreement by Associated Universi-
 11 ties, Inc. The author acknowledges use of the
 12 VLBA under the USNO's time allocation for
 13 some datasets. This work made use of the
 14 Swinburne University of Technology software
 15 correlator, developed as part of the Australian
 16 Major National Research Facilities Programme
 17 and operated under license. This work was
 18 supported by NASA's Space Geodesy Project.

It is my pleasure to thank Yuri Y. Kovalev for thoughtful discussions. The author would like to thank Chris Jacobs for a constructive criticism of early results and an encouragement to perform a quantitative study of the error budget of high frequency absolute radio astrometry.

Facility: VLBA,IVS

Software: PIMA,pSolve

REFERENCES

- Abellán, F. J., Martí-Vidal, I., Marcaide, J. M., & Guirado, J. C. 2018, *A&A*, 614, A74, doi: [10.1051/0004-6361/201731869](https://doi.org/10.1051/0004-6361/201731869)
- Campbell, J., Schuh, H., & Zeppenfeld, G. 1988, in *The Impact of VLBI on Astrophysics and Geophysics*, ed. M. J. Reid & J. M. Moran, Vol. 129, 427
- Charlot, P. 2002, in *International VLBI Service for Geodesy and Astrometry: General Meeting Proceedings*, ed. N. R. Vandenberg & K. D. Baver, 233
- Charlot, P., Boboltz, D. A., Fey, A. L., et al. 2010, *AJ*, 139, 1713, doi: [10.1088/0004-6256/139/5/1713](https://doi.org/10.1088/0004-6256/139/5/1713)
- Charlot, P., Jacobs, C. S., Gordon, D., et al. 2020, *A&A*, 644, A159, doi: [10.1051/0004-6361/202038368](https://doi.org/10.1051/0004-6361/202038368)
- de Witt, A., Jacobs, C. S., Gordon, D., et al. 2023a, *AJ*, 165, 139, doi: [10.3847/1538-3881/aca012](https://doi.org/10.3847/1538-3881/aca012)
- de Witt, A., Jacobs, C. S., Gordon, D., Hunt, L., & Johnson, M. 2023b, in *International VLBI Service for Geodesy and Astrometry 2022 General Meeting Proceedings*, ed. K. L. Armstrong, D. Behrend, & K. D. Baver, 293–297
- Deller, A. T., Tingay, S. J., Bailes, M., & West, C. 2007, *PASP*, 119, 318, doi: [10.1086/513572](https://doi.org/10.1086/513572)
- Deller, A. T., Brisken, W. F., Phillips, C. J., et al. 2011, *PASP*, 123, 275, doi: [10.1086/658907](https://doi.org/10.1086/658907)
- Gordon, D., Jacobs, C., Beasley, A., et al. 2016, *AJ*, 151, 154, doi: [10.3847/0004-6256/151/6/154](https://doi.org/10.3847/0004-6256/151/6/154)
- Gray, J., & Allan, D. 1974, in *28th Annual Symposium on Frequency Control*, 243–246, doi: [10.1109/FREQ.1974.200027](https://doi.org/10.1109/FREQ.1974.200027)
- Hawarey, M., Hobiger, T., & Schuh, H. 2005, *Geophys. Res. Lett.*, 32, L11304, doi: [10.1029/2005GL022729](https://doi.org/10.1029/2005GL022729)

- Kim, J.-Y., Krichbaum, T. P., Broderick, A. E., et al. 2020, *A&A*, 640, A69, doi: [10.1051/0004-6361/202037493](https://doi.org/10.1051/0004-6361/202037493)
- Koryukova, T. A., Pushkarev, A. B., Plavin, A. V., & Kovalev, Y. Y. 2022, *MNRAS*, 515, 1736, doi: [10.1093/mnras/stac1898](https://doi.org/10.1093/mnras/stac1898)
- Kovalev, Y. Y., Lobanov, A. P., Pushkarev, A. B., & Zensus, J. A. 2008, *A&A*, 483, 759, doi: [10.1051/0004-6361:20078679](https://doi.org/10.1051/0004-6361:20078679)
- Kovalev, Y. Y., Petrov, L., Fomalont, E. B., & Gordon, D. 2007, *AJ*, 133, 1236, doi: [10.1086/511157](https://doi.org/10.1086/511157)
- Krasna, H., Gordon, D., de Witt, A., & Jacobs, C. S. 2023, arXiv e-prints, arXiv:2306.09747, doi: [10.48550/arXiv.2306.09747](https://doi.org/10.48550/arXiv.2306.09747)
- Lanyi, G. E., Boboltz, D. A., Charlot, P., et al. 2010, *AJ*, 139, 1695, doi: [10.1088/0004-6256/139/5/1695](https://doi.org/10.1088/0004-6256/139/5/1695)
- Lister, M. L., Aller, M. F., Aller, H. D., et al. 2016, *AJ*, 152, 12, doi: [10.3847/0004-6256/152/1/12](https://doi.org/10.3847/0004-6256/152/1/12)
- Lobanov, A. P. 1998, *A&A*, 330, 79, doi: [10.48550/arXiv.astro-ph/9712132](https://doi.org/10.48550/arXiv.astro-ph/9712132)
- Ma, C., Arias, E. F., Eubanks, T. M., et al. 1998, *AJ*, 116, 516, doi: [10.1086/300408](https://doi.org/10.1086/300408)
- MacMillan, D. S., & Ma, C. 1994, *J. Geophys. Res.*, 99, 637, doi: [10.1029/93JB02162](https://doi.org/10.1029/93JB02162)
- Matveenko, L. I., Kardashev, N.-S., & Sholomitskii, G.-B. 1965, *Soviet Radiophys.*, 461, 461
- Moór, A., Frey, S., Lambert, S. B., Titov, O. A., & Bakos, J. 2011, *AJ*, 141, 178, doi: [10.1088/0004-6256/141/6/178](https://doi.org/10.1088/0004-6256/141/6/178)
- Niell, A., Barrett, J., Burns, A., et al. 2018, *Radio Science*, 53, 1269, doi: [10.1029/2018RS006617](https://doi.org/10.1029/2018RS006617)
- Petit, G., & Luzum, B. 2010, *IERS Technical Note*, 36, 1
- Petrov, L. 2013, *AJ*, 146, 5, doi: [10.1088/0004-6256/146/1/5](https://doi.org/10.1088/0004-6256/146/1/5)
- . 2015, ArXiv e-prints, 1502.06678, <https://arxiv.org/pdf/1502.06678>
- . 2021, *AJ*, 161, 14, doi: [10.3847/1538-3881/abc4e1](https://doi.org/10.3847/1538-3881/abc4e1)
- . 2023, *AJ*, 165, 183, doi: [10.3847/1538-3881/acc174](https://doi.org/10.3847/1538-3881/acc174)
- Petrov, L., de Witt, A., Sadler, E. M., Phillips, C., & Horiuchi, S. 2019, *MNRAS*, 485, 88, doi: [10.1093/mnras/stz242](https://doi.org/10.1093/mnras/stz242)
- Petrov, L., Gordon, D., Gipson, J., et al. 2009, *Journal of Geodesy*, 83, 859, doi: [10.1007/s00190-009-0304-7](https://doi.org/10.1007/s00190-009-0304-7)
- Petrov, L., & Kovalev, Y. Y. 2017, *MNRAS*, 471, 3775, doi: [10.1093/mnras/stx1747](https://doi.org/10.1093/mnras/stx1747)
- Petrov, L., Kovalev, Y. Y., Fomalont, E. B., & Gordon, D. 2011, *AJ*, 142, 35, doi: [10.1088/0004-6256/142/2/35](https://doi.org/10.1088/0004-6256/142/2/35)
- Petrov, L., & Ma, C. 2003, *Journal of Geophysical Research (Solid Earth)*, 108, 2190, doi: [10.1029/2002JB001801](https://doi.org/10.1029/2002JB001801)
- Petrov, L., & Taylor, G. B. 2011, *AJ*, 142, 89, doi: [10.1088/0004-6256/142/3/89](https://doi.org/10.1088/0004-6256/142/3/89)
- Plank, L., Shabala, S. S., McCallum, J. N., et al. 2016, *MNRAS*, 455, 343, doi: [10.1093/mnras/stv2080](https://doi.org/10.1093/mnras/stv2080)
- Plavin, A. V., Kovalev, Y. Y., & Pushkarev, A. B. 2022, *ApJS*, 260, 4, doi: [10.3847/1538-4365/ac6352](https://doi.org/10.3847/1538-4365/ac6352)
- Plavin, A. V., Kovalev, Y. Y., Pushkarev, A. B., & Lobanov, A. P. 2019, *MNRAS*, 485, 1822, doi: [10.1093/mnras/stz504](https://doi.org/10.1093/mnras/stz504)
- Porcas, R. W. 2009, *A&A*, 505, L1, doi: [10.1051/0004-6361/200912846](https://doi.org/10.1051/0004-6361/200912846)
- Pushkarev, A. B., & Kovalev, Y. Y. 2015, *MNRAS*, 452, 4274, doi: [10.1093/mnras/stv1539](https://doi.org/10.1093/mnras/stv1539)
- Rienecker, M., Suarez, M., Todling, R., et al. 2018, *NASA Technical Memorandum*, 104606, 1. <http://gmao.gsfc.nasa.gov/pubs/docs/tm28.pdf>
- Schaer, S. 1999, *Geod.-Geophys. Arb. Schweiz*, Vol. 59,, 59
- Sokolovsky, K. V., Kovalev, Y. Y., Pushkarev, A. B., & Lobanov, A. P. 2011, *A&A*, 532, A38, doi: [10.1051/0004-6361/201016072](https://doi.org/10.1051/0004-6361/201016072)
- Thomas, C. C., MacMillan, D. S., & Le Bail, K. 2024, *Advances in Space Research*, 73, 317, doi: [10.1016/j.asr.2023.07.020](https://doi.org/10.1016/j.asr.2023.07.020)
- Thomas, J. 1980, *JPL Publ.*, 810–005
- Xu, M. H., Savolainen, T., Anderson, J. M., et al. 2022, *A&A*, 663, A83, doi: [10.1051/0004-6361/202140840](https://doi.org/10.1051/0004-6361/202140840)